the folded state (AlB_2 lattice), when the hairpin structures were unfolded, the lattice retained the same basic structure, but with expanded lattice parameters and a substantial loss of long-range order (indicated by a shift to a smaller q values and broadening in the scattering peaks). After a brief annealing period, the lattices transformed into a Cs_6C_{60} structure with long-range order. The reverse transition occurred in a similar manner, where the readjustment of the lattice parameters occurred first (with a corresponding loss of long-range order), followed by reorganization and change in particle coordination number (fig. S4). From this observation, it can be concluded that changes to the bonding nature of the particles occur on a faster time scale than the lattice formation and reorganization processes. Indeed, the bonding mode appears to change nearly instantaneously upon introduction of the appropriate chemical stimuli, whereas the crystallization process for these transmutable particles occurs on a similar time scale and manner as previous PAE constructs (*35*). Taken together, these data indicate that activated transmutable PAEs are nearly indistinguishable from nontransmutable PAEs, enhancing their utility in materials synthesis schemes.

We have used the programmable nature of DNA hairpins and the concept of nanoparticle-based PAEs to develop constructs with bonding behaviors that can be dynamically modulated in response to specific chemical stimuli. The resulting structural plasticity manifested in transmutable particles delineates the power and potential to control PAE architectures, and lays an important foundation for more complex and exotic forms of adaptive matter.

REFERENCES AND NOTES

1. C. A. Mirkin, R. L. Letsinger, R. C. Mucic, J. J. Storhoff, *Nature* **382**, 607–609 (1996).
2. E. V. Shevchenko, D. V. Talapin, N. A. Kotov, S. O'Brien, C. B. Murray, *Nature* **439**, 55–59 (2006).
3. D. V. Talapin, J.-S. Lee, M. V. Kovalenko, E. V. Shevchenko, *Chem. Rev.* **110**, 389–458 (2010).
4. C. Knorowski, S. Burleigh, A. Travesset, *Phys. Rev. Lett.* **106**, 215501 (2011).
5. Z. Tang, Z. Zhang, Y. Wang, S. C. Glotzer, N. A. Kotov, *Science* **314**, 274–278 (2006).
6. M. R. Jones, N. C. Seeman, C. A. Mirkin, *Science* **347**, 1260901 (2015).
7. Y. Wang *et al.*, *Nature* **491**, 51–55 (2012).
8. B. A. Grzybowski, A. Winkleman, J. A. Wiles, Y. Brumer, G. M. Whitesides, *Nat. Mater.* **2**, 241–245 (2003).
9. K. Zhang, X. Zhu, F. Jia, E. Auyeung, C. A. Mirkin, *J. Am. Chem. Soc.* **135**, (2013).
10. P. K. Kundu *et al.*, *Nat. Chem.* **7**, 646–652 (2015).
11. R. J. Macfarlane *et al.*, *Science* **334**, 204–208 (2011).
12. S. Y. Park *et al.*, *Nature* **451**, 553–556 (2008).
13. D. Nykypanchuk, M. M. Maye, D. van der Lelie, O. Gang, *Nature* **451**, 549–552 (2008).
14. R. J. Macfarlane, M. N. O'Brien, S. H. Petrosko, C. A. Mirkin, *Angew. Chem. Int. Ed.* **52**, 5688–5698 (2013).
15. R. J. Macfarlane *et al.*, *Angew. Chem. Int. Ed.* **49**, 4589–4592 (2010).
16. M. R. Jones *et al.*, *Nat. Mater.* **9**, 913–917 (2010).
17. M. N. O'Brien, M. R. Jones, B. Lee, C. A. Mirkin, *Nat. Mater.* **14**, 833–839 (2015).
18. C. Zhang *et al.*, *Nat. Mater.* **12**, 741–746 (2013).
19. Y. Zhang, F. Lu, K. G. Yager, D. van der Lelie, O. Gang, *Nat. Nanotechnol.* **8**, 865–872 (2013).
20. J. D. Brodin, E. Auyeung, C. A. Mirkin, *Proc. Natl. Acad. Sci. U.S.A.* **112**, 4564–4569 (2015).
21. J. Bath, A. J. Turberfield, *Nat. Nanotechnol.* **2**, 275–284 (2007).
22. S. Angioletti-Uberti, B. M. Mognetti, D. Frenkel, *Nat. Mater.* **11**, 518–522 (2012).
23. W. B. Rogers, V. N. Manoharan, *Science* **347**, 639–642 (2015).
24. R. J. Macfarlane, M. R. Jones, B. Lee, E. Auyeung, C. A. Mirkin, *Science* **341**, 1222–1225 (2013).
25. Y. Kim, R. J. Macfarlane, C. A. Mirkin, *J. Am. Chem. Soc.* **135**, 10342–10345 (2013).
26. M. M. Maye, M. T. Kumara, D. Nykypanchuk, W. B. Sherman, O. Gang, *Nat. Nanotechnol.* **5**, 116–120 (2010).
27. N. C. Seeman, *Nature* **421**, 427–431 (2003).
28. B. Yurke, A. J. Turberfield, A. P. Mills Jr., F. C. Simmel, J. L. Neumann, *Nature* **406**, 605–608 (2000).
29. K. Lund *et al.*, *Nature* **465**, 206–210 (2010).
30. P. Yin, H. M. T. Choi, C. R. Calvert, N. A. Pierce, *Nature* **451**, 318–322 (2008).
31. Y. Zhang *et al.*, *Nat. Mater.* **14**, 840–847 (2015).
32. D. Y. Zhang, G. Seelig, *Nat. Chem.* **3**, 103–113 (2011).
33. D. Y. Zhang, E. Winfree, *J. Am. Chem. Soc.* **131**, 17303–17314 (2009).
34. E. Auyeung *et al.*, *Nature* **505**, 73–77 (2014).
35. R. J. Macfarlane *et al.*, *Proc. Natl. Acad. Sci. U.S.A.* **106**, 10493–10498 (2009).

ACKNOWLEDGMENTS

This material is based on work supported by Air Force Office of Scientific Research award FA9550-11-1-0275 (C.A.M., Y.K., R.J.M., M.R.J.) and by the Center for Bio-Inspired Energy Science (CBES), an Energy Frontier Research Center funded by the U.S. Department of Energy, Office of Science, Basic Energy Sciences under award DE-SC0000989-0002 (C.A.M., Y.K.). Y.K., R.J.M., and M.R.J. acknowledge the Ryan Fellowship at Northwestern University. M.R.J. acknowledges the NSF for a graduate research fellowship. Portions of this work were carried out at the DuPont-Northwestern-Dow Collaborative Access Team (DND-CAT) beamline located at Sector 5 of the Advanced Photon Source. DND-CAT is supported by E. I. DuPont de Nemours & Co., Dow Chemical Company, and the state of Illinois.

SUPPLEMENTARY MATERIALS

www.sciencemag.org/content/351/6273/579/suppl/DC1
Materials and Methods
Supplementary Text
Figs. S1 to S4
Tables S1 to S11

10 August 2015; accepted 26 November 2015
10.1126/science.aad2212

MATERIALS SCIENCE

Diamond family of nanoparticle superlattices

Wenyan Liu,[1] Miho Tagawa,[2] Huolin L. Xin,[1] Tong Wang,[3] Hamed Emamy,[4] Huilin Li,[3,5] Kevin G. Yager,[1] Francis W. Starr,[4] Alexei V. Tkachenko,[1] Oleg Gang[1]*

Diamond lattices formed by atomic or colloidal elements exhibit remarkable functional properties. However, building such structures via self-assembly has proven to be challenging because of the low packing fraction, sensitivity to bond orientation, and local heterogeneity. We report a strategy for creating a diamond superlattice of nano-objects via self-assembly and demonstrate its experimental realization by assembling two variant diamond lattices, one with and one without atomic analogs. Our approach relies on the association between anisotropic particles with well-defined tetravalent binding topology and isotropic particles. The constrained packing of triangular binding footprints of truncated tetrahedra on a sphere defines a unique three-dimensional lattice. Hence, the diamond self-assembly problem is solved via its mapping onto two-dimensional triangular packing on the surface of isotropic spherical particles.

The diamond lattice holds a special place among known crystal structures because it is simultaneously simple, yet nontrivial. Tetravalent atoms, such as carbon or silicon, and molecular systems such as water form this lattice under appropriate conditions. However, because of the openness of the lattice, whose volume fraction is only 34% of the hard-sphere limit, higher-density packings frequently prevail. The structure of atomic diamond gives rise to its distinct properties, such as extreme mechanical hardness and a combination of high thermal conductivity and electrical insulation (*1*). The immense historical interest in colloidal diamond lattices is due to the predicted optical response—in particular, its potential application as a full three-dimensional (3D) photonic band gap material (*2*). Yet, building 3D diamond lattices from nano- and microscale particles by means of self-assembly has proven to be remarkably difficult.

Computationally, it was predicted that a delicate balance of isotropic interactions and packing effects might permit the formation of diamond-ordered lattices (*3*–*6*). Indeed, diamond-like structures of isotropically interacting systems were observed in polymers (*7*, *8*) and in a binary system of charged nanoparticles (NPs) (*9*). However, the interactions are typically highly system-specific; thus, it is difficult to generalize such a strategy for the rational assembly of a diamond lattice. Alternatively, engineered anisotropic interactions have been considered. For example,

[1]Center for Functional Nanomaterials, Brookhaven National Laboratory, Upton, NY 11973, USA. [2]Department of Materials Science and Engineering, Nagoya University, Furo-cho, Chikusa-ku, Nagoya 464-8603, Japan. [3]Biology Department, Brookhaven National Laboratory, Upton, NY 11973, USA. [4]Department of Physics, Wesleyan University, Middletown, CT 06459, USA. [5]Department of Biochemistry and Cell Biology, Stony Brook University, Stony Brook, NY 11794, USA.
***Corresponding author. E-mail: ogang@bnl.gov**

precisely truncated tetrahedra were computationally predicted to show a diamond lattice (*10*). Micrometer-scale colloids with tetrahedrally arranged binding sites (*11*), known as "patchy" particles, were developed experimentally (*12–14*). Similar to the tetrahedral symmetry of covalent bonds in atomic systems, such as carbon or silicon, such patchy particles should naturally form diamond lattices. However, recent computational studies proved that at equilibrium, cubic diamond (CD) is degenerate with its hexagonal counterpart when there are only short-range interactions (*12*). Moreover, both these structures compete with an amorphous tetrahedral "liquid," which is thermodynamically favored unless the bonding is highly directional (*15–17*). Free rotation about bonds easily introduces defects, including a mixture of both cubic and hexagonal local structures and leading to a kinetically arrested, disordered state. Thus, tetrahedral motifs on their own are not sufficient for the robust assembly of a diamond crystal. Furthermore, the high sensitivity of the lattices to the position of binding spots imposes exceptionally stringent requirements on the fidelity of particle fabrication. Combined, these complications have hindered the rational assembly of diamond from either micro- or nanoscale particles.

Here, we demonstrate self-assembly of nanoscale cubic diamond superlattices. In our approach, the 3D assembly problem is transformed into a 2D packing problem, bypassing the enumerated challenges. Specifically, our central hypothesis is that the assembly of a diamond structure might be realized without imposing strict requirements on the position, orientation, and shape of binding spots but rather by relying on the self-organization of the binding "footprints" of shaped particles on the surface of isotropic spherical particles (Fig. 1). Although this assembly scenario might seem hopelessly unconstrained, we demonstrate experimentally that our approach leads to the desired diamond structure, drastically streamlining the assembly process. In essence, the engineered topology of interparticle connections encodes a 3D lattice owing to the particular way the footprints of these particles can organize on the surface of the isotropic particles. We show the fabrication of a family of lattices based on the diamond motif using NPs of different types.

Given its distinct selectivity of interactions and structural plasticity, DNA provides a versatile tool for the programmable assembly of finite-sized and extended nanoparticle structures (*18–22*) and close-packed lattices (*23–26*). Our strategy allows for assembly of the diamond family of lattices by using tetrahedral cages, constructed using DNA origami technology (*27*, *28*), as topological linkers between isotropic NPs. Because the size of the origami structure is comparable with a nanoparticle diameter, the tetrahedral linker can be viewed practically as a vertex-truncated tetrahedron (Fig. 1, zoom-in view) with a triangular footprint, which can bind to the isotropic DNA-coated gold NPs via hybridization (Fig. 1).

Isotropic particles and tetrahedral origami self-assemble into an open face-centered cubic (FCC) lattice (Fig. 1, route A). By caging an additional

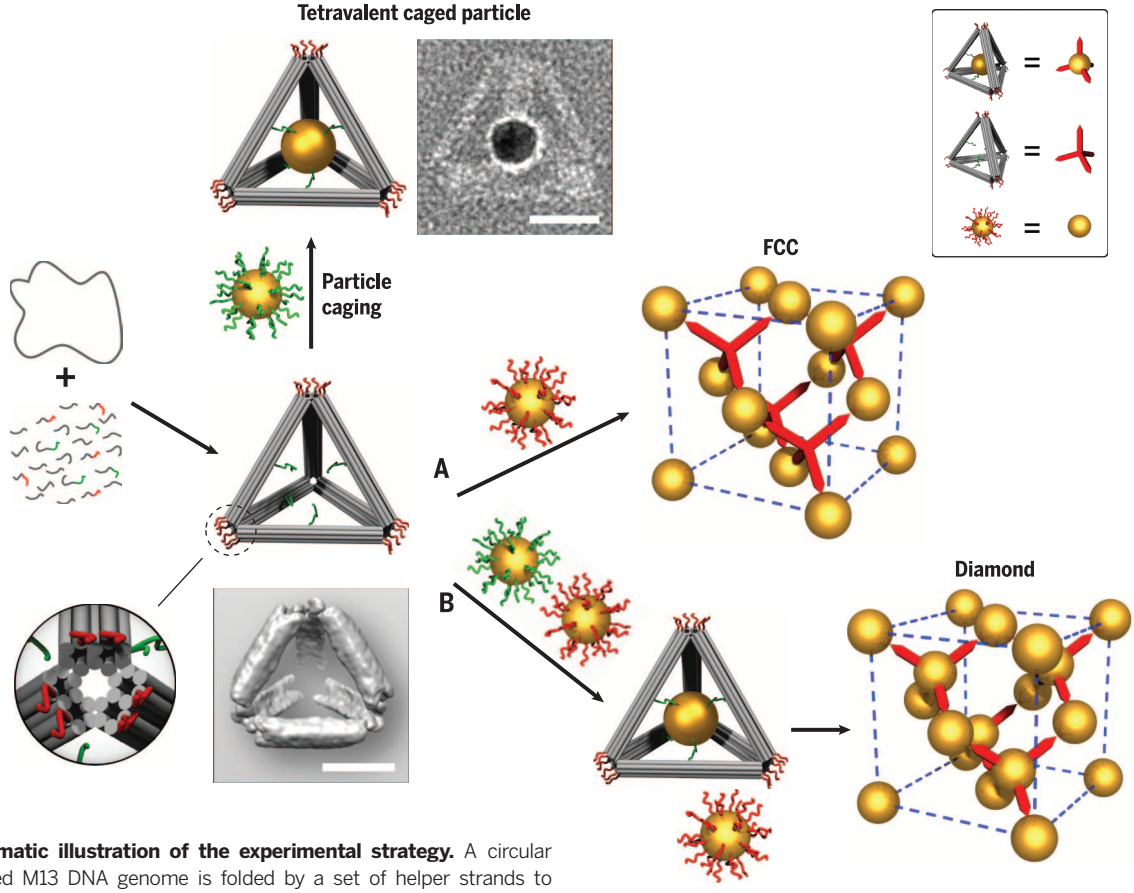

Fig. 1. Schematic illustration of the experimental strategy. A circular single-stranded M13 DNA genome is folded by a set of helper strands to generate a rigid tetrahedral DNA origami cage containing two sets of sticky-ended DNA strands. One set (green) is projected from the inner faces of the edges, functioning as an anchor to encapsulate and hold the guest particle (uniformly coated with green strands) inside the cage; another set (red) is installed at each vertex of the tetrahedral cage, acting as a sticky patch to provide binding to the basis particles (uniformly coated with red strands). (Zoom in) A detailed view of the vertex (truncated) of the tetrahedron cage. The image below the tetrahedron model is a reconstructed cryo-EM density map of the tetrahedron. The guest and the basis particles coated with corresponding complementary DNA can either individually interact with the tetrahedral cages to form tetravalent caged particles and FCC superlattices (route A, empty cages), respectively, or together hybridize with the tetrahedral cages to create diamond crystals (route B, with caged particle). A representative of a constructed tetravalent caged particle is shown in a negative-staining TEM image beside the model. (Top right) A visual definition of the system components for simplified illustration of shown FCC and diamond superlattices. Scale bars, 20 nm.

NP inside each tetrahedron, coassembly with uncaged, isotropic NPs (Fig. 1, route B) instead gives rise to a diamond lattice.

The DNA origami tetrahedron cage is constructed with each of its six edges containing a rigid 10-helix bundle with a length of ≈36 nm and a cross section of ≈9 by 6 nm (Fig. 1). This design creates roughly triangular footprints at the vertices, which contain six dangling single-stranded DNA (ssDNA) (Fig. 1, red strands) for binding of isotropically DNA-coated "basis particles" (melting temperature for DNA links, T_m ≈ 42.3°C). Selected tetrahedral edges are encoded with a different ssDNA sequence that projects toward the interior (Fig. 1, green strands). These internal strands contain ssDNA overhangs (T_m ≈ 48°C) that anchor the "guest particles" (up to ≈26 nm in diameter) inside the tetrahedra, forming tetravalent caged particles (details are provided in the supplementary materials). To achieve single-particle encapsulation, we used gold NPs with a core diameter of 14.5 nm (excluding DNA shell).

We examined the assembled constructs using transmission electron microscopy (TEM). The structure of the DNA origami tetrahedron was resolved by use of cryogenic EM (cryo-EM) and single-particle 3D reconstruction techniques and showed excellent agreement between reconstruction and design (Fig. 1 and fig. S3A). Negative-stain TEM images reveal the high-fidelity positioning of the central guest particle within the tetrahedron, as well as the undistorted cage-particle construct (Fig. 1 and fig. S3B).

We asked whether these nanocomponents—basis isotropic particles, tetrahedra, and tetravalent caged NPs—could be assembled into superlattices. We first tested the assembly of the basis particles (core diameter, 14.5 nm) with the tetrahedral cages, whose vertices host complementary ssDNA (Fig. 1, route A). We mixed and annealed the two components and probed the assembled structure by means of in situ small-angle x-ray scattering (SAXS). The 2D scattering pattern and the associated structure factor $S(q)$ revealed a series of sharp scattering peaks. The ratio of the positions of the peaks (q^n/q^1) matches 1: $\sqrt{4/3}$: $\sqrt{8/3}$: $\sqrt{11/3}$: 2: $\sqrt{16/3}$..., indicating the formation of a well-defined FCC lattice (Fig. 2, A and C). Our modeling of $S(q)$—which accounts for particle size, origami dimensions, and lattice correlation length (a description of the SAXS modeling is available in the supplementary materials)—is in excellent agreement with the experimental curve (*29*) (Fig. 2C, top channel, and fig. S10). How the basis particles are linked by DNA tetrahedra in the FCC lattice is illustrated in Fig. 2D. The interparticle distance d is 71.9 nm, which is consistent with the spacing calculated from the sizes of our components (a detailed calculation is provided in the supplementary materials). Formation of the FCC lattice per se is noteworthy, given the rotational freedom of the tetrahedra when they interact with isotropic particles in the lattice.

The FCC structure provides a platform for the assembly of a CD lattice because the unit cell of diamond can be viewed as a FCC cell with four additional objects located at (1/4, 1/4, 1/4), (3/4, 3/4, 1/4), (1/4, 3/4, 3/4), and (3/4, 1/4, 3/4), the exact centers of the tetrahedra (Fig. 1). Thus, to assemble a CD lattice, we used isotropic gold NPs of 14.5-nm core diameter both as the basis particles and the guest particles. Using a one-pot slow annealing process, we mixed an equal molar ratio of two types of NPs coated with different DNA (sequence designs are provieded in the supplementary materials) (table S1). Because of the separation of melting temperatures of anchoring strands inside tetrahedra and at the vertices, the lattice assembly occurs in two distinct steps

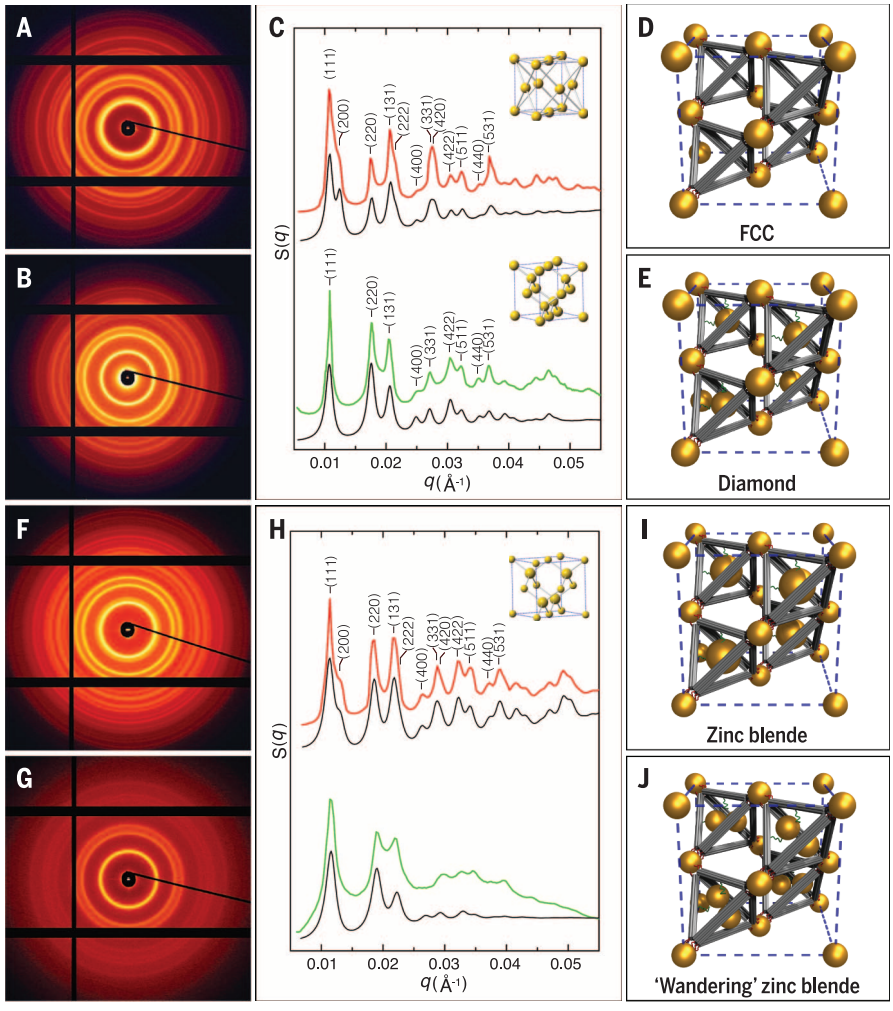

Fig. 2. SAXS characterization of the diamond family of nanoparticle superlattices. (**A**) 2D SAXS pattern of the FCC superlattices constructed with basis particles (core diameter, 14.5 nm) and tetrahedral DNA origami cages. (**B**) 2D SAXS pattern of the diamond superlattices formed from basis particles (core diameter, 14.5 nm) and tetravalent caged particles (core diameter, 14.5 nm). (**C**) Integrated 1D patterns. The top channel shows experimental (red) and calculated (black) 1D SAXS patterns for the FCC crystals. The bottom channel shows experimental (green) and calculated (black) 1D SAXS patterns for the diamond crystals. (Insets) Standard FCC (top) and diamond unit cells (bottom). (**D**) Unit cell model of the assembled FCC superlattice. (**E**) Unit cell model of the constructed diamond crystal. (**F**) 2D SAXS pattern of the zinc blende lattices constructed with basis particles (core diameter, 8.7 nm) and tetravalent caged particles (core diameter, 14.5 nm). (**G**) 2D SAXS pattern of the wandering zinc blende lattices formed from basis particles (core diameter, 8.7 nm) and guest particle pairs (core diameter, 8.7 nm) caged inside the tetrahedra. (**H**) Integrated 1D patterns. The top channel shows experimental (red) and modeled (black) structure factors, $S(q)$, for the zinc blende crystals (inset, standard zinc blende unit cell). The bottom channel shows experimental (green) and modeled (black) structure factors for the wandering zinc blende lattices. (**I**) Unit cell model of the assembled zinc blende superlattice. (**J**) Unit cell model of the wandering zinc blende lattice, where caged particle pairs have no specific orientation in the tetrahedra.

(Fig. 1): The guest particles with DNA shells complementary to inner (green) strands were first trapped inside the cages, forming the tetravalent caged particles; these caged particles subsequently hybridized with the basis particles to form lattices. The SAXS reveals a crystalline organization with a substantial degree of long-range order, as evident from >15 sharp diffraction peaks (Fig. 2, B and C). The peak positions correspond to $q^n/q^1 \approx 1$: $\sqrt{8/3}$: $\sqrt{11/3}$: $\sqrt{16/3}$: $\sqrt{19/3}$: $\sqrt{8}$: 3..., which is in precise agreement with a cubic diamond lattice. The measured lattice constant is 100.7 nm ($2\pi\sqrt{3}/q^1$), which is consistent with the 43.7-nm center-to-center distance between the basis and caged particles ($a\sqrt{3}/4$) and the 71.2-nm distance between the two basis particles ($a/\sqrt{2}$). The agreement between the calculated and experimental $S(q)$ profiles further confirms the formation of a well-ordered diamond lattice (Fig. 2C, bottom channel, and fig. S11), whose unit cell model is shown in Fig. 2E.

On the basis of the same strategy, we built two variant lattices in the CD family: a zinc blende lattice and another lattice for which there is no known atomic analog. The zinc blende lattice was obtained by replacement of the 14.5-nm basis particles in the CD with smaller 8.7-nm particles. Our assembled zinc blende structures exhibited excellent long-range crystalline order (Fig. 2, F and H, and fig. S4). Again, we observed a precise correspondence between experimental and modeled scattering curves (Fig. 2H, top channel, and fig. S12), confirming the formation of the designed zinc blende lattice shown in Fig. 2I.

To assemble the second variety of the CD family lattice, we used a pair of 8.7-nm core diameter guest NPs for caging inside the tetrahedra and NPs, with a core diameter of 8.7 nm as the basis particles. The tetrahedron interiors were decorated with two additional anchoring strands, for a total of 6 ssDNA. The reduced NP size and the increased anchor points allow for the caging of two particles within one DNA origami tetrahedron (fig. S8). We call the assembled structure a "wandering" zinc blende lattice because the guest particles have greater positional freedom. Its x-ray diffraction pattern is similar to that of the canonical zinc blende structure, but of a lower quality (Fig. 2, G and H). The absence of higher-order diffraction peaks is likely due to the random occupancy of the two distinct but equally sized particles within the tetrahedra. Our SAXS modeling in this case assumed that the two caged particles were randomly and isotropically oriented. The modeled profile approximately matches the experimental curve (Fig. 2H, bottom channel, and fig. S13), supporting our predicted structural organization (Fig. 2J). This binary organization is notable because one nanocomponent (the basis particle) is well positioned, whereas another component (the guest particle pair) has considerable local freedom.

We also applied cryo-scanning transmission electron microscopy (cryo-STEM) to directly visualize the assembled lattices. The cryo-STEM images of the assembled diamond-family superlattices are shown in Fig. 3, plunge-frozen from their native liquid environment (figs. S5 to S7). In this experiment, the image formation is dominated by Rutherford scattering from the atomic nuclei in the sample. Thus, the image reflects the projected atomic mass contrast, in which areas with gold would have intensities higher than those of ice. As can be seen in Fig. 3, A, E, and I, respectively, all three assemblies—FCC, diamond, and zinc blende—exhibit well-ordered lattices of NPs. The enlarged images of each self-assembled superlattice shown in Fig. 3, B, F, and J, respectively, match the [110] projections of their corresponding models (Fig. 3, C, G, and K). To draw an analogy between our self-assembled superlattices and naturally occurring atomic crystals, the atomic-resolution images of platinum (FCC), silicon (CD), and zinc telluride (zinc blende) along the [110] zone axis are shown in Fig. 3, D, H, and L, respectively. The self-assembled nanoparticle superlattices (Fig. 3, B, F, and J) closely match their atomic analogs.

The mechanism of formation for these diamond-family lattices is quite intricate. Over short ranges, the energy of the FCC lattice is identical to that of the hexagonally closed packed (HCP) lattice, as well as their derivatives such as CD, zinc blende, and hexagonal diamond (HD). The CD and HD lattices are indistinguishable from the point of view of the nearest-neighbor coordination because in both scenarios, tetrahedra can connect to four particles. Furthermore, whereas the DNA tetrahedron binds anisotropically, the basis particles interact isotropically. In other words, there is seemingly substantial freedom in the way in which the tetrahedra can attach to a particle surface.

Below, we present a simple model that explains the formation of the observed superlattices. This model attributes their robust self-assembly to the specific truncated architecture of the DNA cages (Fig. 4A), not merely to their overall tetrahedral symmetry. In this model, steric and electrostatic repulsion between the cages is represented

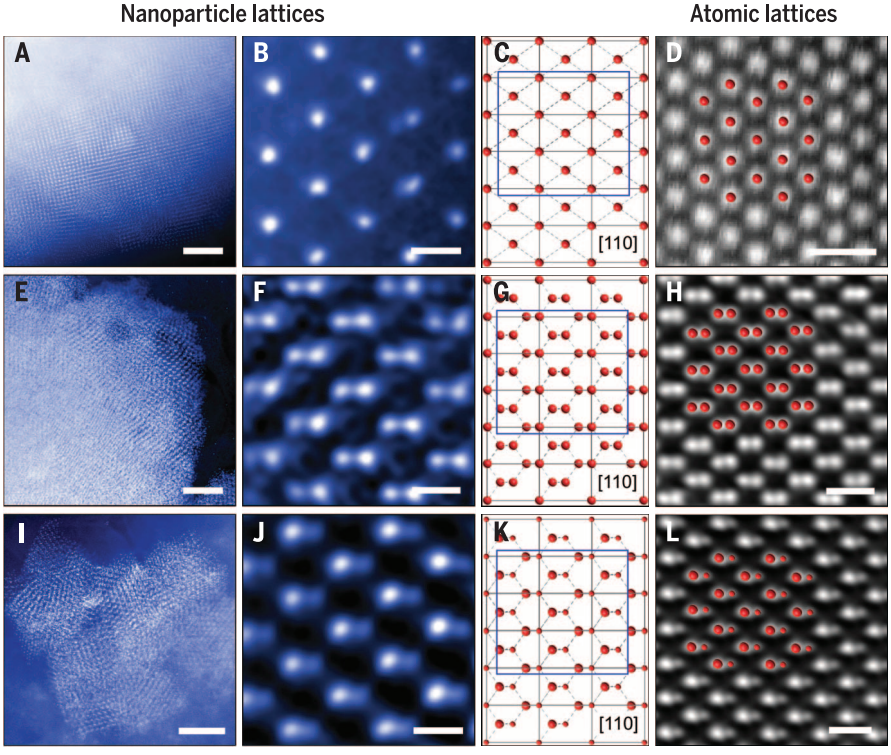

Fig. 3. Cryo-STEM images of the diamond family of nanoparticle superlattices. (**A** and **B**) FCC superlattices constructed with basis particles (core diameter, 14.5 nm) and tetrahedral DNA origami cages. (A) Low-magnification image. (B) High-magnification image taken along the [110] zone axis. (**C**) Schematic projection of a FCC lattice along [110] zone axis. (**D**) High-angle annular dark-field scanning–STEM (HAADF-STEM) image of platinum viewed in the [110] direction. (**E** and **F**) Diamond superlattices formed from basis particles (core diameter, 14.5 nm) and tetravalent caged particles (core diameter, 14.5 nm). (E) Low-magnification image. (F) High-magnification image taken along the [110] zone axis. (**G**) Schematic projection of a diamond lattice along [110] zone axis. (**H**) HAADF-STEM image of silicon viewed along the [110] direction. (**I** and **J**) Zinc blende lattices constructed with basis particles (core diameter, 8.7 nm) and tetravalent caged particles (core diameter, 14.5 nm). (I) Low-magnification image. (J) High-magnification image taken along the [110] zone axis. (**K**) Schematic projection of a zinc blende lattice along [110] zone axis. (**L**) HAADF-STEM image of zinc telluride viewed along the [110] direction. The match between the nanoparticle lattices and the atomic analogs confirms the successful assembly of the diamond family of nanoparticle superlattices. Scale bars, (A), (E), and (I), 500 nm; (B), (F), and (J), 50 nm; (D), (H), and (L), 0.5 nm.

by the rigid-body interaction between the truncated tetrahedra.

Each tetrahedron binds to a spherical particle, through a large "footprint" on its surface, as shown in Fig. 4A (red triangle), owing to its truncation. This footprint is approximately an equilateral triangle, with side length $b \approx 10\sigma \approx 20$ nm (where $\sigma \approx 2$ nm is the diameter of a DNA duplex). For the combination of sizes used in our experiments, the hard-core constraint between truncated tetrahedra is equivalent to the requirement of no overlap between their respective footprints on the spherical particle surface. In this way, we map the 3D assembly of NPs and cages onto the 2D arrangement of triangles on a spherical surface. In this mapping, the sphere corresponds to a NP with its DNA shell, including the double-stranded DNA (dsDNA) segments formed upon hybridization with the cages. The diameter D of this sphere in our experiments is $D \approx 35$ nm, out of which 14.5 nm is the gold core and 10 nm is an approximate thickness of the ssDNA/dsDNA shell.

Shown in Fig. 4B are three examples of the triangle-on-a-sphere arrangements that correspond to three plausible superlattices: FCC (with 1:1 NP to DNA cage ratio, as shown in Fig. 4C), HCP, and FCC (with 1:2 ratio). FCC (1:1) clearly corresponds to the most compact footprint arrangement. Whereas FCC (1:2) can be discarded as geometrically impossible for our size ratio ($b/D \approx 0.6$), in the case of HCP, the noncompact footprint arrangement translates into a significant entropic cost compared with that of FCC (1:1). As we show, this entropy is associated primarily with rotational degrees of freedom of DNA cages (supplementary materials), and the corresponding correction to the free energy per cage is

$$\Delta F \approx 2kT \ln\left(\frac{b^* - b}{b^*/2 - b}\right)$$

Here, $b^* = \sqrt{6D^2 - 8b^2}$. In our case ($b/D \approx 0.6$), a substantial thermodynamic advantage to FCC is given by $\Delta F \approx 2.8kT$. In addition, electrostatics and steric repulsions between cages would also favor FCC over HCP.

To further validate this conclusion, we performed numerical simulations of ground-state structures of the DNA-origami–linked nanoparticle structures using a coarse-grained representation, previously validated experimentally (*30*). We examined configurations of basis particles linked by tetrahedra in either FCC or HCP arrangements. In the FCC (or CD) configuration, the faces of tetrahedra are aligned (Fig. 4D), whereas in the HCP (or HD), only alternating planes align (Fig. 4E). Consequently, the longer-ranged repulsion between edges results in an energy gap that favors FCC (Fig. 4F). The size of this gap is related to the screening length of the potential. Thus, the medium-ranged repulsion of the truncated tetrahedral linkers provides another thermodynamic driving force to stabilize FCC (or CD) over otherwise similar structures.

Thus, we have demonstrated how packing of linker footprints on the surface of isotropic nanoparticles can enforce the formation of a desired lattice, including the experimental realization of the elusive diamond superlattice and its derivatives.

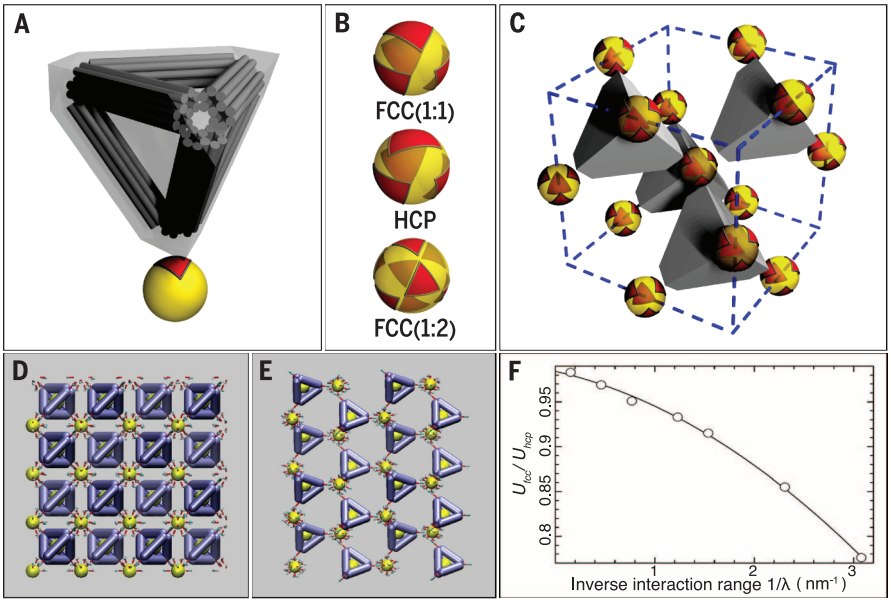

Fig. 4. Mechanism of the formation of the FCC and diamond superlattices. (**A**) Model of the binding interaction between the DNA tetrahedral cage and the nanoparticle. The DNA tetrahedral cage was modeled as a truncated tetrahedron completely encompassing the cage. The binding of the tetrahedral cage to the nanoparticle leaves an equilateral triangular footprint on the particle surface. (**B**) Triangle-on-a sphere arrangement. (Top) For the FCC superlattice (with 1:1 NP to DNA cage ratio). (Middle) For the HCP superlattice. (Bottom) The FCC superlattice (with 1: 2 NP to DNA cage ratio). (**C**) Illustration of the FCC lattice of isotropic particles formed because of their connection by truncated tetrahedra in the regime shown in (B) [top, FCC (1:1)]. (**D**) Snapshot of the simulation for FCC (or cubic diamond) configuration. (**E**) Snapshot of the simulation for HCP (or hexagonal diamond) configuration. (**F**) Ratio of electrostatic energy for FCC (or CD) and HCP (or HD) organizations, based on screened Coulombic interactions between the negatively charged DNA bundles that comprise the tetrahedral cages. The lower energy of FCC organizations is favored.

REFERENCES AND NOTES

1. J. E. Field, *Rep. Prog. Phys.* **75**, 126505 (2012).
2. E. Yablonovitch, *J. Opt. Soc. Am. B* **10**, 283–295 (1993).
3. A. V. Tkachenko, *Phys. Rev. Lett.* **89**, 148303 (2002).
4. É. Marcotte, F. H. Stillinger, S. Torquato, *J. Chem. Phys.* **138**, 061101 (2013).
5. A. Jain, J. R. Errington, T. M. Truskett, *Phys. Rev. X* **4**, 031049 (2014).
6. A. P. Hynninen, J. H. J. Thijssen, E. C. M. Vermolen, M. Dijkstra, A. van Blaaderen, *Nat. Mater.* **6**, 202–205 (2007).
7. B. Capone, I. Coluzza, F. LoVerso, C. N. Likos, R. Blaak, *Phys. Rev. Lett.* **109**, 238301 (2012).
8. E. L. Thomas *et al.*, *Macromolecules* **19**, 2197–2202 (1986).
9. A. M. Kalsin *et al.*, *Science* **312**, 420–424 (2006).
10. P. F. Damasceno, M. Engel, S. C. Glotzer, *ACS Nano* **6**, 609–614 (2012).
11. Y. Wang *et al.*, *Nature* **491**, 51–55 (2012).
12. F. Romano, E. Sanz, F. Sciortino, *J. Chem. Phys.* **132**, 184501 (2010).
13. Z. Zhang, A. S. Keys, T. Chen, S. C. Glotzer, *Langmuir* **21**, 11547–11551 (2005).
14. N. Kern, D. Frenkel, *J. Chem. Phys.* **118**, 9882–9889 (2003).
15. F. Smallenburg, L. Filion, F. Sciortino, *Nat. Phys.* **10**, 653–657 (2014).
16. F. W. Starr, F. Sciortino, *Soft Matter* **10**, 9413–9422 (2014).
17. W. Dai, C. W. Hsu, F. Sciortino, F. W. Starr, *Langmuir* **26**, 3601–3608 (2010).
18. C. Zhang *et al.*, *ACS Nano* **8**, 1130–1135 (2014).
19. J. Zheng *et al.*, *Nano Lett.* **6**, 1502–1504 (2006).
20. D. Nykypanchuk, M. M. Maye, D. van der Lelie, O. Gang, *Langmuir* **23**, 6305–6314 (2007).
21. S. Y. Park *et al.*, *Nature* **451**, 553–556 (2008).
22. A. Kuzyk *et al.*, *Nature* **483**, 311–314 (2012).
23. R. J. Macfarlane *et al.*, *Science* **334**, 204–208 (2011).
24. T. Vo *et al.*, *Proc. Natl. Acad. Sci. U.S.A.* **112**, 4982–4987 (2015).
25. M. T. Casey *et al.*, *Nat. Commun.* **3**, 1209 (2012).
26. F. Lu, K. G. Yager, Y. Zhang, H. Xin, O. Gang, *Nat. Commun.* **6**, 6912 (2015).
27. P. W. K. Rothemund, *Nature* **440**, 297–302 (2006).
28. S. M. Douglas *et al.*, *Nature* **459**, 414–418 (2009).
29. K. G. Yager, Y. G. Zhang, F. Lu, O. Gang, *J. Appl. Cryst.* **47**, 118–129 (2014).
30. C. Chi, F. Vargas-Lara, A. V. Tkachenko, F. W. Starr, O. Gang, *ACS Nano* **6**, 6793–6802 (2012).

ACKNOWLEDGMENTS

Research carried out at the Center for Functional Nanomaterials, Brookhaven National Laboratory, was supported by the U.S. Department of Energy, Office of Basic Energy Sciences (contract DE-SC0012704). H.L. was supported by a National Institutes of Health R01 grant (AG029979). F.W.S. was supported by National Institute of Standards and Technology award 70NANB13H202. We thank K. Kisslinger for help with sample preparation for TEM and J. Neitzel for the contribution to the simulation work.

SUPPLEMENTARY MATERIALS

www.sciencemag.org/content/351/6273/582/suppl/DC1
Materials and Methods
Supplementary Text
Figs. S1 to S15
Tables S1
References (*31*–*42*)
Movie S1

7 August 2015; accepted 18 December 2015
10.1126/science.aad2080